

Studies of Electron Cloud Growth and Mitigation in a Field Free Environment Using Retarding Field Analyzers

J.R. Calvey, M.G. Billing, J.V. Conway, G. Dugan, S. Greenwald, Y. Li, X. Liu,
 J.A. Livezey, J. Makita, R.E. Meller, M.A. Palmer, S. Santos, R.M. Schwartz,
 J. Sikora, C.R. Strohman, CLASSE, Cornell University, Ithaca, NY, USA
 S. Calatroni, G. Rumolo, CERN, Geneva, Switzerland
 K. Kanazawa, Y. Suetsugu, KEK, Ibaraki, Japan
 M. Pivi, L. Wang, SLAC, Menlo Park, CA, USA

(Dated: June 26, 2012)

Over the course of the past three years, the Cornell Electron Storage Ring (CESR) has been reconfigured to serve as a test accelerator (CESRTA) for next generation machines, in particular for the ILC damping ring. A significant part of this program has been the installation of diagnostic devices to measure and quantify the electron cloud effect, a potential limiting factor in these machines. In particular, several Retarding Field Analyzers (RFAs) have been installed in CESR. These devices provide information on the local electron cloud density and energy distribution, and have been used to evaluate the efficacy of different cloud mitigation techniques. This paper will provide an overview of RFA results obtained in a drift environment. Understanding these results provides a great deal of insight into the behavior of the electron cloud.

PACS numbers: 29.20.db, 52.35.Qz, 29.27.-a

I. INTRODUCTION

The electron cloud effect is a well known phenomenon in particle accelerators, in which a high density of low energy electrons builds up inside the vacuum chamber. These electrons can cause a wide variety of undesirable effects, including emittance growth and beam instabilities. The cloud can be seeded by photoelectrons generated by synchrotron radiation, or by ionization of residual gas. The collision of these “primary” electrons with the beam pipe can then produce one or more (“secondary”) electrons, depending on the secondary electron yield (SEY) of the material. If the average SEY is greater than unity, the cloud density will grow exponentially.

Electron cloud has been observed in many existing facilities, and is expected to be a major limiting factor in next generation machines. It is of particular concern in the damping rings of next generation electron-positron colliders, which will produce a large amount of synchrotron radiation and require very small emittances.

In 2008, the Cornell Electron Storage Ring (CESR) was reconfigured to study issues related to the design of International Linear Collider (ILC) damping ring, including electron cloud. A significant component of this program, called CESR Test Accelerator (CESRTA) was the installation of several retarding field analyzers (RFAs) throughout the ring, in drift, dipole, quadrupole, and wiggler field regions. This paper will summarize results obtained from drift RFAs.

A. Retarding Field Analyzers

A retarding field analyzer consists of three main components: holes drilled in the beam pipe to allow electrons

to enter the device; a “retarding grid,” to which a voltage can be applied, rejecting electrons with less than a certain energy; and a positively biased collector, to capture any electrons which make it past the grid [1]. If space permits, additional (grounded) grids can be added to allow for a more ideal retarding field. In addition, the collectors of most RFAs used in CESRTA are segmented to allow characterization of the geometry of the cloud build-up. Thus a single RFA measurement provides information on the local cloud density, energy, and transverse distribution. Several different styles of RFA have been deployed in drift locations in CESR; Table I gives a list of the styles discussed in this paper.

We have used RFAs to probe the local behavior of the cloud in different locations in CESR, in the presence of different mitigation schemes. Most of the data presented here is one of two types: “voltage scans,” in which the retarding voltage is varied (typically from +100 to -250V) while beam conditions are held constant, or “current scans,” in which the retarding grid is set to a positive voltage (typically 50V), and data is passively collected while the beam current is increased.

The primary advantage of CESR as a test accelerator is its flexibility. At CESRTA, we have been able to study the electron cloud under a wide variety of beam conditions, varying the number of bunches, bunch current, bunch spacing, beam energy, and species. As described in Section VI, this is very helpful for independently determining the photoelectron and secondary electron properties of the instrumented chamber. Table II lists some of the more common (but by no means only) beam parameters used for electron cloud mitigation studies with RFAs.

TABLE I: Drift RFA styles deployed in CESR

Type	Grids	Collectors	Grid Transparency
Thin Test	1	1	40%
APS	2	1	90%
Insertable I	2	5	40%
Insertable II	3	11	90%
Thin	1	9	90%

TABLE II: Common beam conditions for electron cloud mitigation studies

Parameter	Typical Values	Units
Number of bunches	9, 20, 30, 45	-
Bunch current	.75, 1.25, 2.8, 3.8, 10	mA
Bunch spacing	4, 14, 280	ns
Species	Electron, positron	-
Beam energy	2.1, 4, 5.3	GeV

II. INSTRUMENTATION

A rough chronology of drift RFA measurements at CESRTA is as follows:

- **2008:** Initial bench tests and in-situ measurements on a single collector “thin test” RFA show that this type of RFA can produce sensible results. These are described in [2].
- **Early 2009:** Test chambers are installed in the 14W and 14E arcs of CESR. Measurements in the 14W section confirm that an “Inesertable” style RFA gives results comparable to the well understood “APS” style [2]. Measurements at 14E provide our first mitigation comparison- TiN coated copper vs bare copper (Section IV).
- **Late 2009:** “Thin” style RFAs are installed in short test sections at 15W and 15E. These locations will provide the majority of our drift mitigation comparisons.
- **2010:** Chambers with different coatings are tested at 15W and 15E. Also, a long NEG coated chamber, instrumented with APS style RFAs, is installed in our L3 straight section.
- **2011 - 2012:** Mitigation comparisons continue at 15E and 15W, now with “Insertable II” style RFAs, which have somewhat improved performance relative to the thin style. A new round of bench measurements are performed to characterize our drift RFAs in more detail.

Each of these experiments is explained in detail below.

A. Initial Bench Tests

The “thin test” style RFA (Table I) was designed to test whether RFAs could perform in vacuum chambers

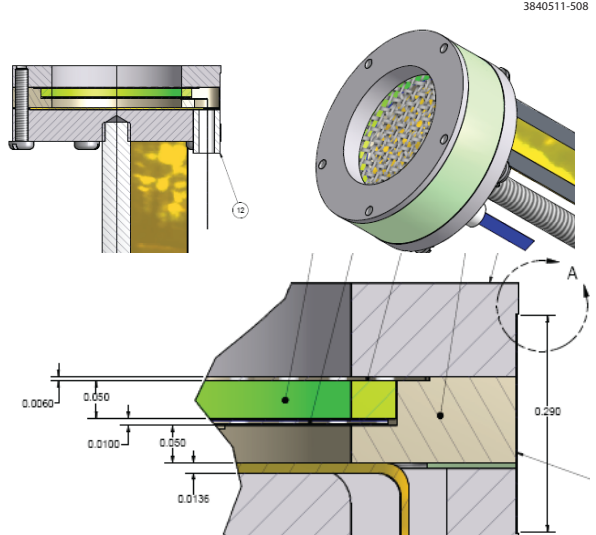


FIG. 1: The basic retarding field analyzer structure for use in vacuum chambers with limited external aperture. Two variants of this design have been tested. In the first variant (shown), two grids are employed in front of a collector made of copper-clad Kapton. In the second variant, the front grid is replaced by a block of copper with a hole pattern of the same type as implemented in the walls of the CESRTA diagnostic wiggler vacuum chambers. In these designs, the layers are supported by a ceramic structure with an interlayer spacing of approximately 1 mm.

where detector space is severely limited due to magnet apertures. Thus the design minimizes the thickness of the structure, although this has performance implications for the device. In particular, the maximum retarding voltage will be limited to a few hundred volts with a somewhat degraded energy resolution. A self supporting 0.006" thick stainless steel with an etched bi-conical hole structure (0.007" diameter holes with a 0.01" pitch) was chosen for the grids while the electron collector pads were laid out on copper-clad Kapton sheet using standard printed circuit board fabrication techniques. These layers can be supported with machined ceramic or PEEK structures.

The specific RFA structure that was used both for bench testing with an electron gun and for beam testing in CESR is shown in Figure 1. Typically, the grid layers are vacuum-coated with a thin gold layer (several hundred nm) to reduce their secondary electron yield. Operating voltages are typically 20-100 V on the collector and retarding voltages in the range of +100 to -300 V.

B. 14W and 14E Test Sections

Upon the removal of the CESR-c SCWs from CESR arcs, two EC experimental sections were created on both east and west sides of CESR. At the former locations of CESR-c SCW-doublets, a pair of copper beam pipes were

installed for each SCW-doublet, as shown in Figure 2. The longer copper beam pipe of the two was coated with TiN thin film for half of its length (while the other half remained bare copper). Two segmented RFAs were installed at each end of this EC test chamber to compare EC-intensity on TiN coated copper to the bare copper. Since these EC-test chambers reside in long vacuum sectors in CESR, they are not intended to be frequently replaced.

C. 15W and 15E Mitigation Comparison Chambers

To allow frequent exchanges of EC test chambers, while minimizing impact to the accelerator operations, two very short experimental regions were created in place of two CESR-c SCWs in the Q15W and Q15E locations in the arcs. Additional RF-shielded UHV gate valves were installed at these two regions, so that only a very small portions (approximately 8.2 m in length) of the CESR vacuum, which includes only one dipole bending chamber and a short straight, may be vented to N₂ in order to replace a test chamber in the short straight. Figure 3 are photographs of the Q15 experimental regions, as they were created during the summer 2008 CESR shutdown. Many test chambers were rotated through the Q15 test regions during the CESRTA program, as described in Section IV.

These regions have been used extensively for the study of various passive coatings, including TiN, amorphous carbon (a-C) and diamond-like carbon (DLC), in order to evaluate their EC-suppression effectiveness, as well as their vacuum performance in an intense SR environment. These studies are in collaborations with the CLIC/CERN and the KEK groups.

To fulfill the above research goals, an experimental chamber design was developed to allow the characterization of the EC growth and decay and its transverse distribution within the vacuum chamber for different wall surfaces and with progressive beam-processed conditions. The design of this EC experimental chamber is illustrated in Figure 4. The beam pipe is machined from standard CESR aluminum (Type 6063-T6 alloys) extrusions. For EC measurements an RFA port and a set of 4 shielded pickup detectors (see [3] for details) are added to the chamber.

The RFA housing is machined from a separated block of explosion-bonded aluminum-to-stainless steel material, and is welded to the cutout on top of the beam pipe. The lower face of the RFA housing matches curvature of the beam pipe aperture. Small holes are drilled through the three milled flat surfaces, connecting the RFA port to the beam space. These RFA holes are 0.75 mm in diameter and ~2.5 mm in thickness, and are grouped into three ‘segments’ on each flat, with each segment containing 44 holes (thus a total of 9×44 = 396 holes). The segmented hole pattern allows the sampling of the transverse distribution of the EC in the beam pipe. The dimensions of

the RFA holes are chosen to ensure no significant leakage of the beam’s RF fields into the detector signals, while maximizing the transparency of the RFA to the vacuum chamber.

Over the past 3-year CESRTA program, five Q15 experimental chambers were fabricated and tested in the Q15W and Q15E regions. Among these experimental chambers, four types of interior surfaces and two types of RFA designs were tested. The four types of tested surfaces are: bare aluminum (as it was originally extruded), amorphous carbon coatings (coated by CERN/CLIC), TiN coating (by Cornell) and diamond-like carbon coating (by KEK). Table III summarizes these test chambers. Figure 5 shows a typical installation of these experimental chambers.

Two generations of RFA designs were used on the Q15 experimental chambers. The first generation was adapted from the thin RFA design used for a CESR dipole chamber (Fig. 6). As listed in Table III, this thin-style design was used in the first four test chambers, including a bare aluminum chamber, two amorphous carbon coated chambers, and a TiN coated chamber (in Runs #1 and #2).

Photos, taken during the assembly of the thin-style RFA into a Q15 chamber, are given in Figure 7. In the thin-style design, UHV-compatible Kapton tape with Silicone adhesive (Model # KAP-TP-36-2S from Accu-Glass Products, Inc.) was used to electrically isolate the flexible RFA collector circuit. We performed independent vacuum evaluation of the Kapton tape, by measuring vacuum total pressure as well as the RGA spectrum of the tape at 230°C. The vacuum tests indicated no unusual outgassing from the tape, thus qualifying their applications in CESR vacuum system. However, traces (~6% mono-layer) of silicon was measured on the a-C coated samples that were present during the 150°C bakeout of the first a-C coated RFA chamber. This trace of silicon contamination may have contributed to a much higher measured SEY than was observed on the witness sample. In the second a-C coated chamber, although the amount of Kapton tape was reduced by more than 90%, an even higher level of silicon contamination and higher SEY was still measured on the witness a-C coated coupons! However, as described in section IV, these chambers still showed good performance *in situ*.

Thus a second generation of the Q15 RFA design was developed, to be completely adhesive-free. This fully insertable RFA assembly is illustrated in Figure 8. The insertable RFA consists of three high-transparency copper meshes, with the bottom mesh grounded and 2nd and 3rd meshes permitted to be individually biased. These meshes are nested in frames made of PEEK, and connected through Kapton-coated wires. The flexible circuit RFA collector was replaced with copper bars. The insertable RFA was installed in the 5th Q15 test chamber, with diamond-like carbon coating. To provide cross calibration between the two RFA designs, the thin-style RFA in the TiN coated test chamber was replaced with

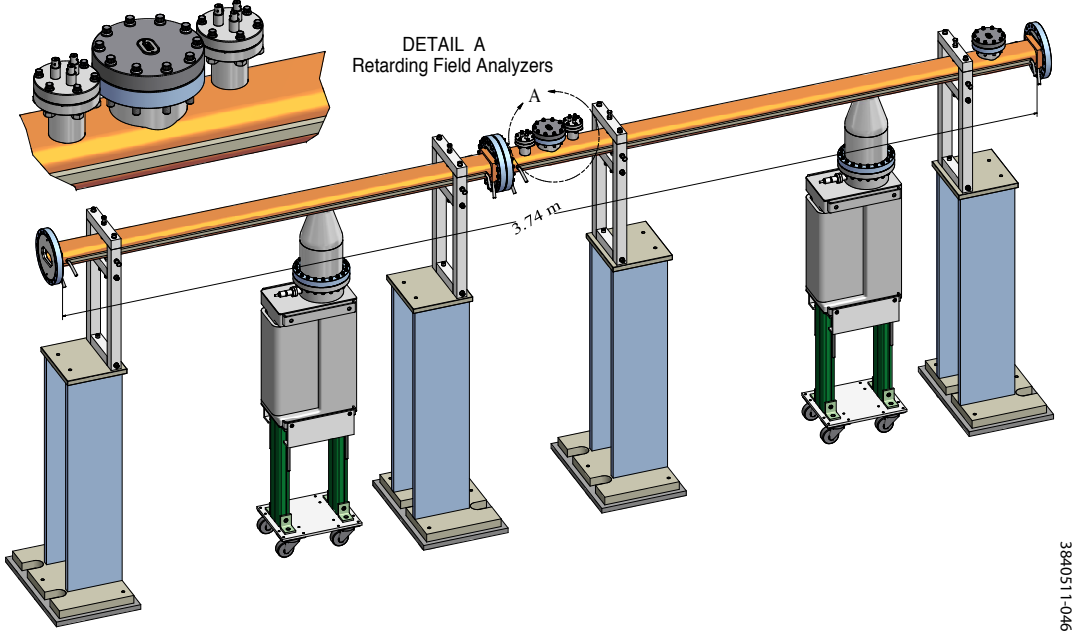


FIG. 2: EC experiment section created by the removal of SCW-doublets in CESR.

TABLE III: Summary of Q15W and Q15E Experimental Vacuum Chambers (VCs)

VC#	Surface	RFA Style	Test Period	Location	Note
1	Aluminum Run#1	Thin	2009.07~2009.11	Q15W	Reference surface
	Aluminum Run#2	Thin	2010.04~2010.08	Q15W	Reference surface
2	TiN Run#1	Thin	2009.12~2010.04	Q15E	TiN coating via DC sputtering at Cornell
	TiN Run#2	Thin	2010.08~2011.01	Q15W	Same chamber as above
	TiN Run#3	Insertable	2011.02~2011.07	Q15W	Cross-comparison of two RFA designs
3	a-C#1 Run#1	Thin	2009.7~2010.04	Q15W	a-C coating via DC sputtering at CERN
4 a	a-C#2 Run#1	Thin	2010.04~2011.01	Q15E	a-C coating via DC sputtering at CERN
	a-C#2 Run#2	Insertable	2011.07~present	Q15W	Cross-comparison of two RFA designs
5	DL-C	Insertable	2011.02~present	Q15E	DL-C coating via pulsed DC plasma-CVD, supplied by KEK

^aIn this round of RFA installation, efforts were made to reduce adhesive Kapton tape by at least 90%, and the preinstallation bakeout temperature was reduced to 120°C. However, higher δ and higher trace levels of Si were still observed in the witness coupon!

the insertable one. (Refer to Table III)

D. NEG Test Section

A Ti/Zr/V non-evaporable getter (NEG) thin film [4] has been shown to have a low SEY, after its activation at elevated temperatures under vacuum. The activated NEG coating also has the benefit of providing vacuum pumping. A NEG-coated test chamber, equipped with EC diagnostics, was build and tested in the drift section

of the L3 Experimental Region. To prevent rapid saturation of the activated NEG thin film in the test chamber from residual gases in the surrounding beam pipes, the test chamber was sandwiched between two 1-m long NEG coated beam pipes, as shown in Figure 9. The EC test chamber was equipped with three APS-style RFAs at three angles and RF-shielded pickup on the top (see Figure 10. All three chambers were made of stainless steel (Type 304L).

The NEG thin film deposition was done by SAES Getter Inc., via a DC magnetron sputtering method, using



FIG. 3: Two very short EC experimental section in CESR arcs (shown in at Q15E, TOP). Bottom left (Q15W) and right (Q15E) are closeup photos for the two place-holder chambers in these test sections.

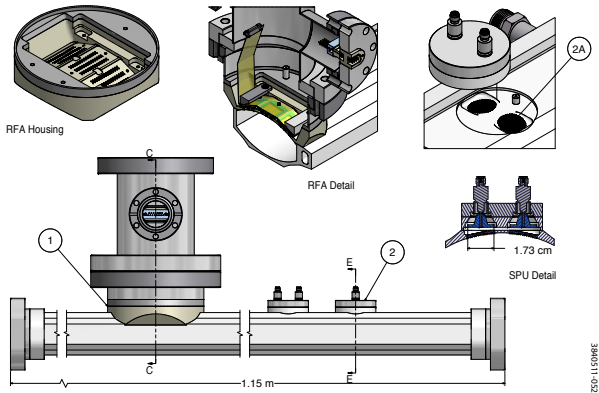


FIG. 4: Q15 EC Test Chamber, equipped with a RFA (1) and 4 SPUs (2)

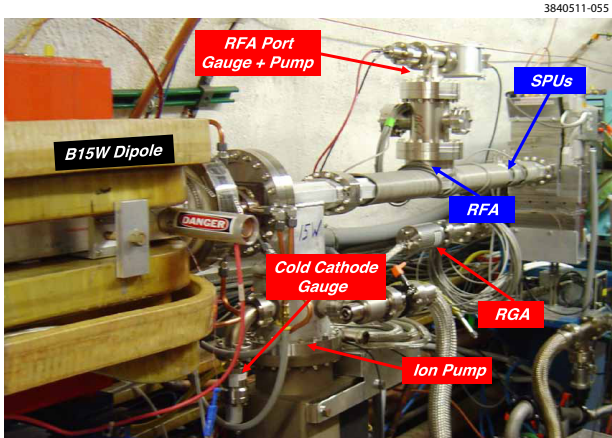


FIG. 5: A Q15 EC experimental chamber installed at Q15W in CESR.

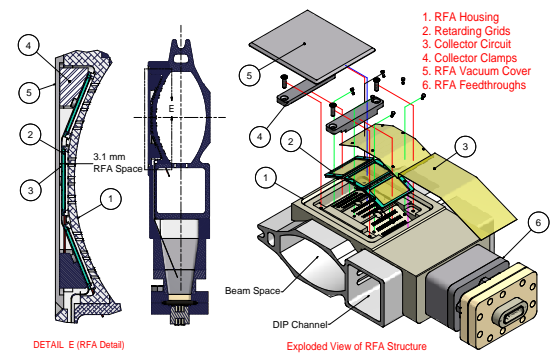


FIG. 6: RFA design detail for a CESR dipole chamber.

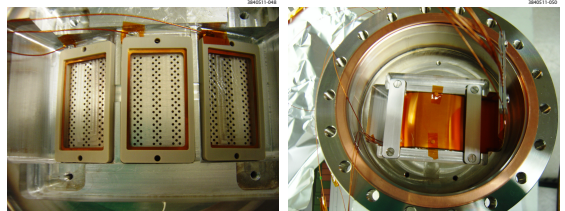


FIG. 7: Photos showing installation process of Cornell Dipole thin-style RFA in Q15 experimental chamber. LEFT photo shows three high transparency retarding grids mounted. The RFA holes are clearly visible through the fine meshes of the grids. RIGHT photo shows the collector circuit pinned into location, and clamped down with aluminum bars.

twisted wires of Ti, Zr and V as the sputtering cathode. The thickness of the NEG thin film is $\sim 2 \mu\text{m}$. During the coating process, all diagnostic instruments (RFAs and SPU) were removed. A 24-hr 150°C bakeout was carried out to the NEG-coated beam pipe string, with RFAs and SPU inserted, prior to the installation in the L3 Experimental Region. These NEG-coated beam pipes replaced the PEP-II EC text chambers in the drift section of L3 region.

Fiber-glass insulated heating tapes were wrapped around and along the NEG beam pipe string for the activation. Six large bore (11-inch diameter) Helmholtz coils, evenly spaced along the beam pipe string (shown in Figure 11) replace the normal solenoid winding, found on most of the CESR beam pipes, as the solenoid windings are incompatible with the high temperature heating required during the activation of the NEG coating. The NEG coating was activated at 250°C for a duration of 24 to 48 hours. After each venting of the L3 region and to preserve pumping capacity of the NEG thin film, the activation was normally carried out following the initial period of beam conditioning of the beam pipes.

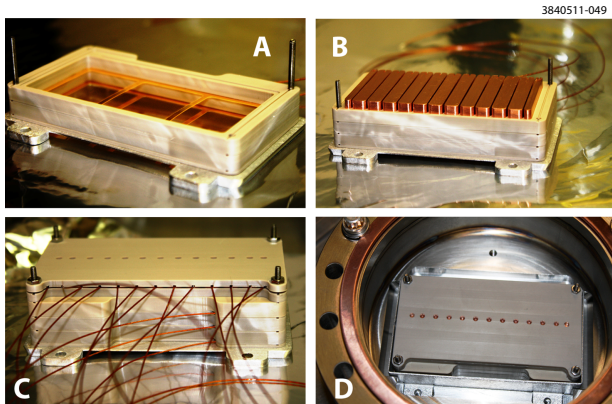


FIG. 8: Photo of insertable RFA used in Q15 experimental chambers. (A) High transparency gold-coated copper meshes are mounted in PEEK frames; (B) RFA collector, made of copper bars are mounted on top of the meshes; (C) after soldering all connections (including 2 grids and 13 collectors), finish the RFA assembly with a PEEK top cap; (D) the insertable RFA mounted in the RFA port of a test chamber (wires not shown here for clarity)

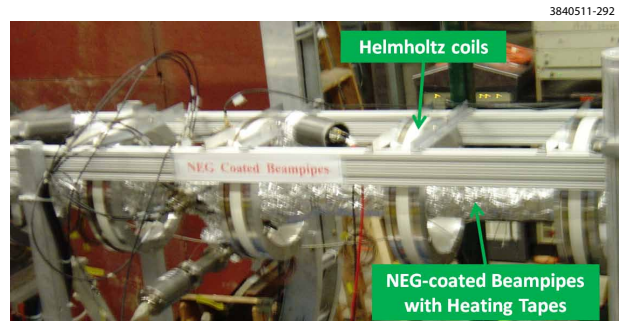


FIG. 11: NEG coated beam pipes Installed in L3 with Helmholtz Coils.

III. DATA ACQUISITION SYSTEM

A modular high voltage power supply and precision current monitoring system has been designed to support RFA measurements at multiple locations around CESR. A block diagram is shown in Figure ???. Each HV supply contains two four-quadrant grid supplies and a single unipolar collector supply. The standard grid supply can operate from -500 V to +200 V and can provide -4.4 mA to 2.4 mA at 0 V. The unipolar collector supply can operate from 0V to 200 V and is rated for 50 mA. A digital control loop is used to set and stabilize the output of the each supply with a feedback resolution of 60 mV. The feedback is specially configured to enable high precision current measurements while the feedback loop is quiescent. Upon receipt of a voltage command, the HV control sets the voltage and allows it to stabilize. At that point, all feedback corrections are suspended for a 20 second data acquisition window. The controls for the two grid and single collector supplies in a full HV supply are configured to make this quiescent period simultaneous. The RFA data boards distribute bias voltages to the detector elements (up to 17) and measure the current flow in each. The current is measured by an isolation amplifier looking at a series resistor (selectable as 1, 10, 100 or 1000 k Ω) in the high side of the circuit with the output going to a 16-bit digitizer. The various resistors correspond to full scale ranges of 10000, 1000, 100, and 10 nA. The finest resolution is 0.15 pA. The readout system is in a 9U VMEbus crate with a custom P3 backplane that distributes bias voltages to the databoards. This backplane is divided into three segments, each with its own HV power supply. A common controller board controls all of the HV supplies and incorporates voltage and current trip capability. The entire crate is connected to the CESR control system through the local fieldbus. Data acquisition code running on the CESR control system is capable of running energy scans and continuous current monitoring by way of this communications path. Separate data acquisition servers operate for each of the crates deployed in CESR. These servers are controlled through a MATLAB based GUI (Fig. 12), which also allows for

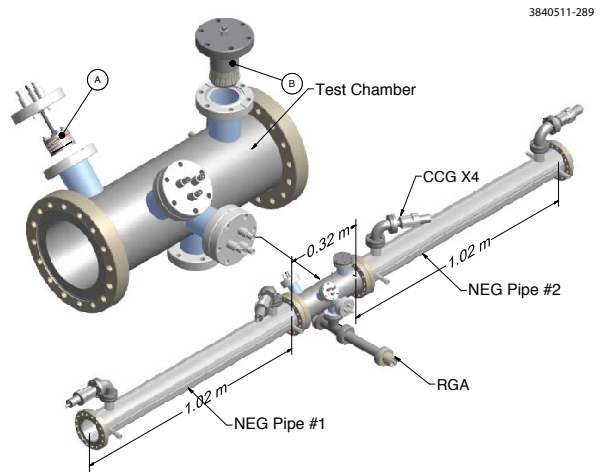


FIG. 9: Vacuum chambers with NEG thin film coating in the drift section of the L3 Experimental Region. The test chamber included: (A) 3 units of APS-style RFAs; (B) RF-shielded pickup assembly supplied by LBNL.

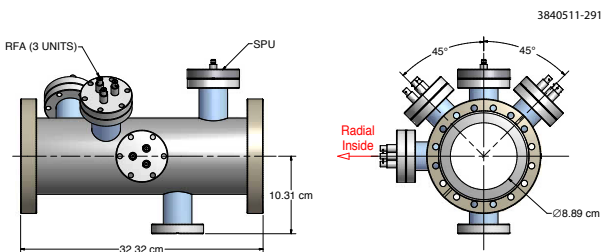


FIG. 10: EC Diagnostic chamber with NEG thin film coating.

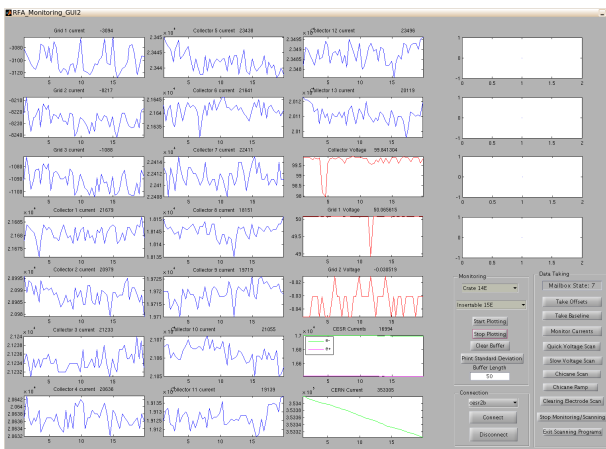


FIG. 12: MATLAB GUI, showing real time readout of the grid and collector currents and voltages, as well as the beam current.

real time monitoring of any RFA.

IV. MEASUREMENTS

Many of our earliest detailed measurements were done with “Insertable I” style RFAs (Table I). Fig 13 shows an example of a voltage scan done with one of these RFAs, in typical CESRTA beam conditions. It plots the RFA response as a function of collector number and retarding voltage. Roughly speaking this is a description of the transverse and energy distribution of the cloud. In this example, the signal is fairly broad across all five collectors, indicating that the cloud density is not strongly peaked around the beam. It also falls off quickly with retarding voltage, indicating that the majority of cloud particles have low energy. The RFA signal is expressed in terms of current density in nA/mm^2 , normalized to the transparency of the RFA beam pipe and grids. In principle, this gives the time averaged electron current density incident on the beam pipe wall. The beam conditions are given as “1x45x1.25 mA e+, 14ns, 5.3 GeV.” This notation, which will be used throughout this section, indicates one train of 45 bunches, with 1.25mA/bunch (1mA = 1.6×10^{10} particles), with positrons, 14ns spacing, and at beam energy 5.3GeV.

Fig 14 compares a current scan measurement done with two adjacent RFAs, one in a bare Copper chamber, and one in a TiN coated Copper chamber. Here we compare the average collector current density in the two detectors, as a function of beam current, and find that it is lower in the coated chamber by a factor of two.

“Thin” style RFAs (Table I) were developed to fit inside the aperture of a CESR dipole, but they have also been deployed in drift regions. These RFAs have since been replaced by “Insertable II” style detectors, which have more collectors and can support higher voltages. Example measurements done with both of these RFA

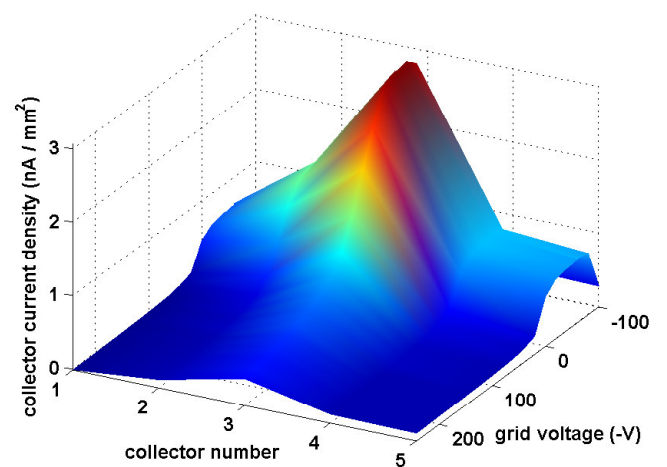


FIG. 13: RFA voltage scan with an insertable segmented drift RFA in a Cu chamber, 1x45x1.25 mA e+, 14ns, 5.3 GeV

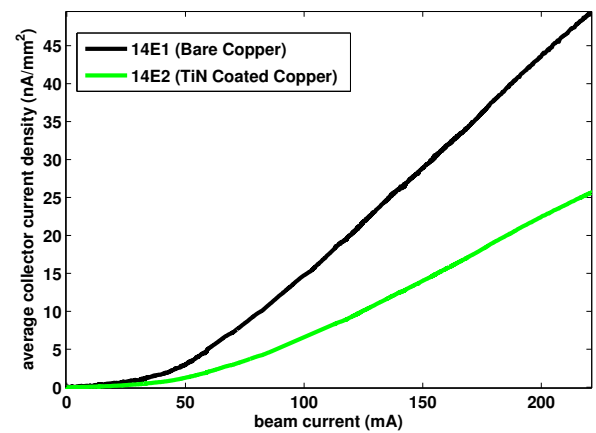


FIG. 14: Comparison of insertable drift RFAs, 1x20 e+, 5.3GeV, 14ns

styles, in a TiN coated chamber, can be found in Fig. 15.

A. MITIGATION COMPARISONS

We have installed RFAs in arc drift sections adjacent to the 15E and 15W quadrupoles in CESR. The photon flux for a positron beam at 15W is about twice that of 15E, and vice versa for an electron beam. Measurements have been taken at both locations with TiN and amorphous carbon coatings, as well as with an uncoated aluminum chamber. In addition, a chamber with diamond-like carbon (DLC) coating has been installed at 15E. By comparing measurements taken at the same location in CESR, we ensure the comparisons can be made under identical beam conditions, including photon flux. Figs. 16 through 18 compare the RFA signal with each of these coatings for

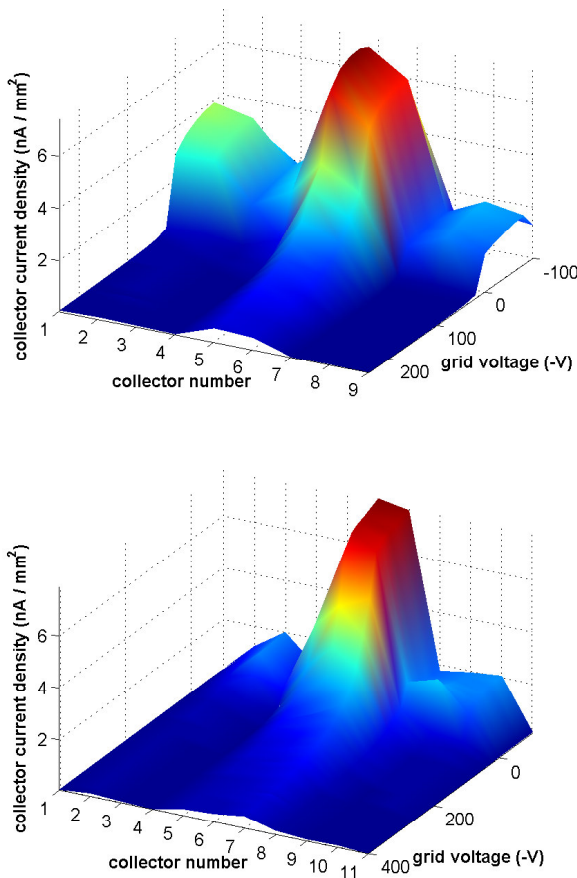


FIG. 15: Example voltage scans with thin (left) and insertable (right) style drift RFAs in the same location. Both are TiN coated, beam conditions are 1x45x1.25mA, 5.3GeV, 14ns.

typical sets of CESRTA beam conditions. We have generally found that data taken with 20 bunches of positrons at high current shows the biggest difference between the different chambers. It is under these conditions that we expect to be most sensitive to the peak secondary electron yield (δ_{max}).

All coated chambers show a sizeable reduction in signal when compared to uncoated aluminum. After extensive processing, both TiN and amorphous carbon coated chambers show similar mitigation performance. The details of the small difference between 15E and 15W (where in one case TiN appears slightly better and in the other amorphous carbon does) require further analysis to understand fully.

Diamond-like carbon may perform better than other coatings at very high beam current. It should be noted that bench measurements of the Secondary Electron Yield (SEY) of DLC have found that the material can retain charge if bombarded with a sufficiently high electron flux, thus modifying the apparent SEY performance. This effect may also be influencing the in situ measurements presented here.

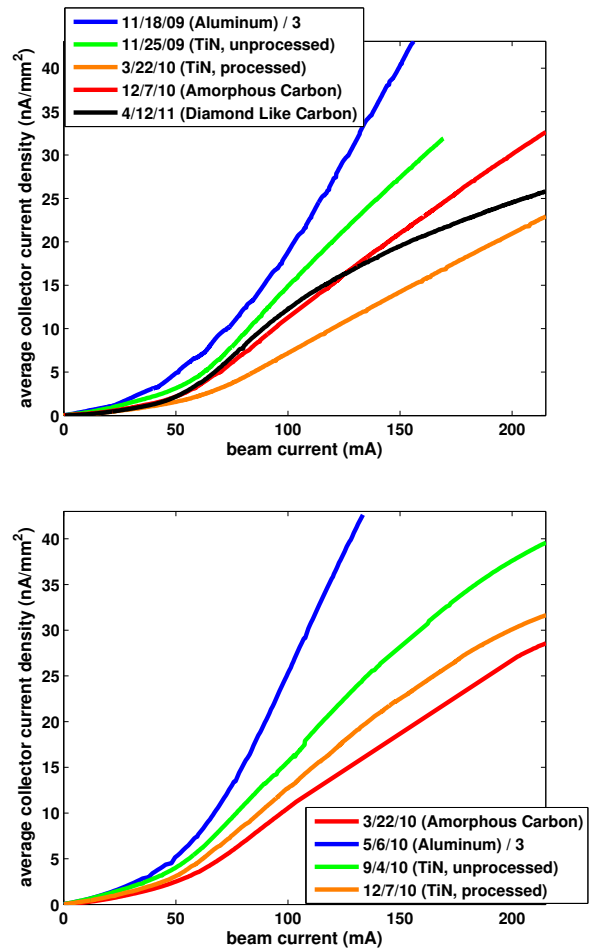


FIG. 16: Comparison of different beam pipe coatings, 15E (top), and 15W (bottom) drift RFAs. Plots show average collector signal vs beam current for **20 bunches of positrons** with **14ns** spacing, at beam energy **5.3GeV**. Note that the aluminum chamber signals are divided by 3.

We have also installed a NEG coated chamber in our L3 straight region. This chamber is instrumented with three single collector RFAs, located at different azimuthal positions. Fig. 19 compares the current measured by one of these RFAs on several different dates, corresponding to different states of activation and processing of the NEG coating. It was observed that both activation and initial processing reduced the signal measured by this RFA. After a CESR down (during which the NEG was activated again), the signal rose somewhat, but it processed back down to its minimum value after a few months of beam time. The other two detectors showed a similar trend.

V. RFA MODELING

To understand the measurements described above on a more quantitative level, one needs a way of translating an RFA measurement into physical quantities relating to

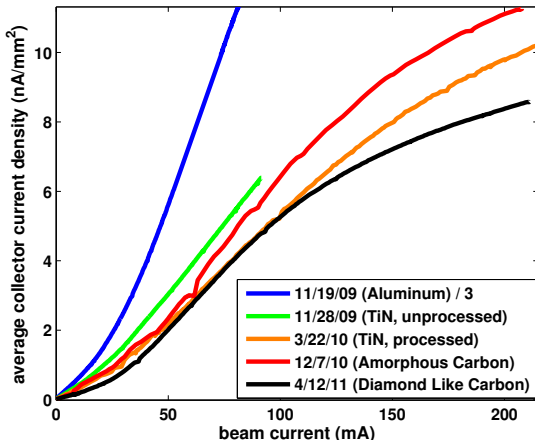


FIG. 17: Comparison of different beam pipe coatings, 15E (top) and 15W (bottom) drift RFAs. Plots show average collector signal vs beam current for **20 bunches of electrons** with **14ns** spacing, at beam energy **5.3GeV**. Note that the aluminum chamber signals are divided by 3.

the development of the electron cloud. To bridge this gap, accurate models of both the cloud development and the RFA itself are required. The former task is handled by a well validated cloud simulation code such as POSINST [5], which tracks the motion of cloud particles during and after the passage of a bunch train. The latter is the subject of this section.

Previous efforts to analyze RFA data [6] have relied on post-processing the POSINST “death certificates” file, which contains a record of all the macroparticle-wall collisions that took place during the simulation. Recently, models for a few different RFA types have been integrated into the code, and a file containing the simulated RFA signals is automatically produced by the simulation. In addition to being much faster and using less disk space than the post-processing method, the integrated model is more self-consistent, since it allows for charge that enters into the RFA to be taken out of the cloud in the vacuum chamber.

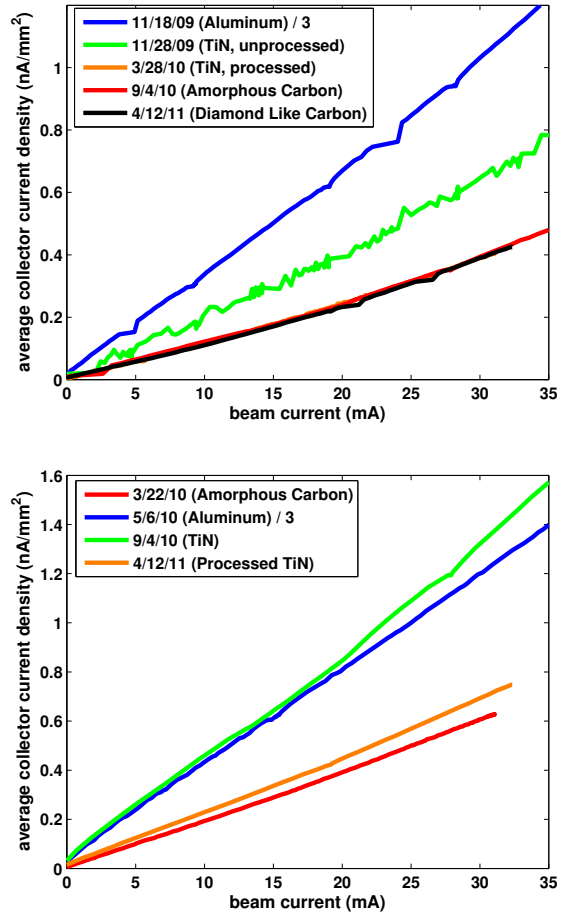


FIG. 18: Comparison of different beam pipe coatings, 15E (top) and 15W (bottom) drift RFAs. Plots show average collector signal vs beam current for **9** equally spaced (**280ns**) bunches of **positrons**, at beam energy **5.3GeV**. Note that the aluminum chamber signals are divided by 3.

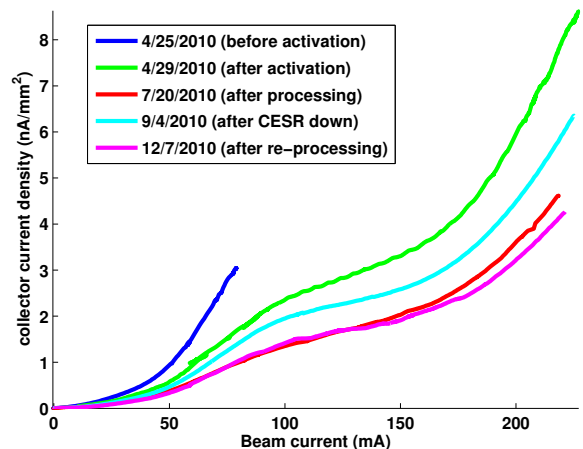


FIG. 19: NEG RFA comparison, 1x20 e+, 5.3GeV, 14ns

The integrated RFA model is implemented as a special function that is called before the normal secondary emission code. It checks to see if the macroparticle is in the region covered by the RFA. If so, a certain fraction of the macroparticle charge, which depends on the incident angle and energy (as well as the overall beam pipe transparency), is added to the collector signal. The charge is binned by energy and transverse position, simulating the energy and position resolution of the RFA. The macroparticle then has its charge reduced by the amount that went into the RFA.

To aid in the development of our model, we constructed a bench experiment to test the response of a test RFA under controlled conditions. The system consists of an electron gun, which can produce a monoenergetic and roughly uniform beam of electrons, aimed at a test RFA. The RFA includes a faceplate with holes drilled in it to mimic the vacuum chamber, a high efficiency (nominally 92%) retarding grid, and a collector. We are able to independently control the voltage and read the current on the collector, grid, and faceplate, as well as a top ring surrounding the faceplate. To do a measurement with this system, we set the electron gun to a specific energy, and adjust the focusing of the gun until the beam just covers the faceplate (i.e. until no current is observed on the top ring). We can then study the response of the RFA as a function of incident energy (by changing the gun energy) and angle (by changing the distance from the gun to the RFA). An example retarding voltage scan, done with 100 nA of a 200 eV beam, is shown in Fig. 20 (green dots). The collector was set to 100 V, and the faceplate to 0 V. A few things are worth noting about the measurement:

- The collector signal is mostly flat for a retarding voltage between 0 and -200 V, as expected for a monoenergetic beam.
- When the grid voltage is positive, there is a strong enhancement of the signal, caused by the production of low energy secondary electrons in the faceplate holes.
- The signal does not immediately disappear with -200 V on the retarding grid, but drops off steadily, reaching zero current at -230 V. This effect is caused by focusing of the beam by the non-ideal field of the grid, which allows electrons with energy slightly lower than the retarding voltage to slip by.
- The current on the retarding grid is strongly negative for most of the scan, meaning its average secondary electron yield is much higher than unity.

We have also developed a specialized particle tracking code, which tracks the motion of electrons through a model of the RFA. This model includes a detailed replica of the faceplate, grid, and collector, shown in Fig. 21. It allows for the production of secondary electrons on both the faceplate and grid. The secondary emission code is

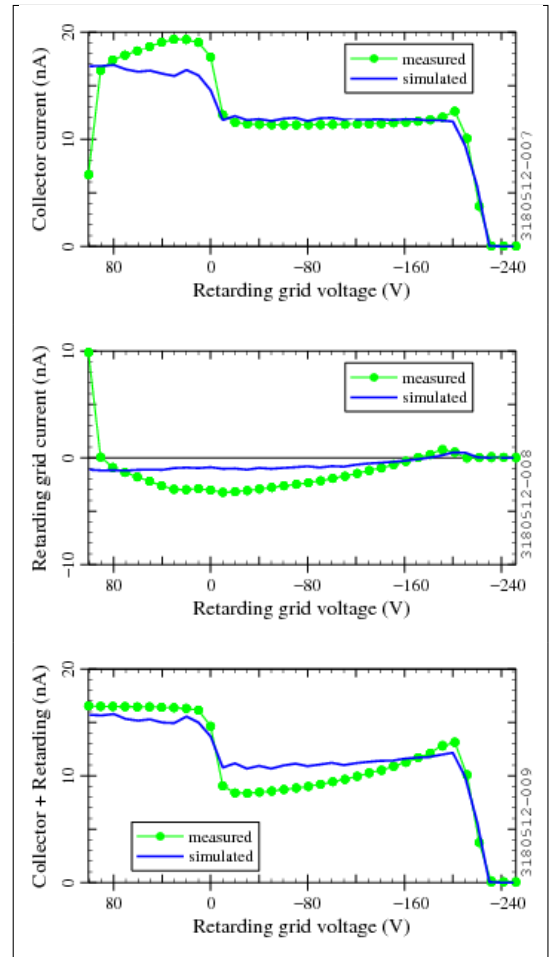


FIG. 20: Simulated (blue lines) and measured (green dots) test RFA signals. The plots show the current in the collector (top), retarding grid (middle), and their sum (bottom).

a simplified version of the one used in POSINST, and includes both elastic and “true” secondaries. The RFA model also features a realistic map of the electric fields produced by the grid and collector, generated by the electrostatic calculation tool Opera 3D.

Fig. 20 compares the results of a bench measurement with the model. It shows excellent agreement for the collector signal for negative grid voltage, including the focusing effect described above. The model underestimates both the collector signal at positive voltage and the magnitude of the signal on the grid. However, it matches the sum of the two fairly well, implying that the discrepancy arises from an underestimation of the number of secondaries produced by the grid. These secondaries are repelled to the faceplate when the voltage is negative, but attracted to the grid when the voltage is positive. To account for this effect, the fits described below use the sum of the grid and collectors when comparing the signal at positive voltage.

Overall, the style of RFA modeled in our test setup is fairly well understood.

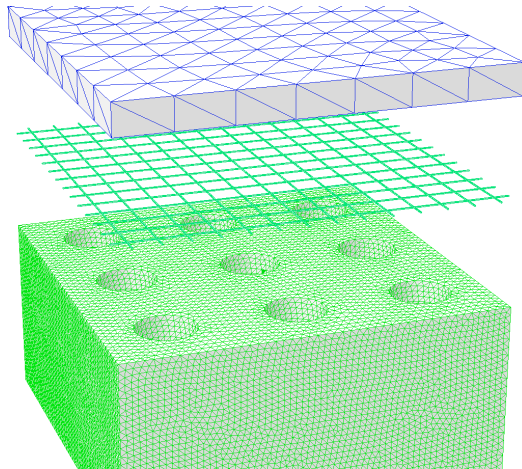


FIG. 21: Opera 3D model of a typical drift RFA, showing (from top to bottom) the collector, thin retarding grid, and faceplate/vacuum chamber.

VI. SIMULATIONS

The large quantity of RFA data obtained during the CESRTA program necessitates a systematic method for detailed analysis. To this end, an RFA model has been incorporated into POSINST, enabling much faster analysis of the simulation. This model includes most of the effects described in the previous section, including the enhancement of the collector signal at positive voltage due to secondaries from the beam pipe holes and retarding grid. The overall goal of the analysis is, given a set of voltage scan data, to find a set of simulation parameters that bring data and simulation into as close to agreement as possible.

A chi squared analysis has been employed to accomplish this. In short, we want to minimize χ^2 , as defined in Eq. 1. Here \mathbf{y} a vector containing the difference between the data and a nominal simulation, \mathbf{X} is the Jacobian matrix, and β is the a vector containing the change in each of the parameters under study. \mathbf{W} is a diagonal matrix whose elements are $\frac{1}{\sigma_i^2}$, where σ_i is the error on data point i . Note that both the data and simulation can contribute to this error. The value of β which will minimize χ^2 is given in Eq. 2. Once a new set of parameter values is obtained, the process can be repeated with this new set as the “nominal” values. This method will generally need to be iterated a few times before it converges on the actual minimum value of χ^2 .

$$\chi^2 = (\mathbf{y} - \mathbf{X}\beta)^T \mathbf{W} (\mathbf{y} - \mathbf{X}\beta) \quad (1)$$

$$\beta = (\mathbf{X}^T \mathbf{W} \mathbf{X})^{-1} \mathbf{X}^T \mathbf{W} \mathbf{y} \quad (2)$$

There are many subtleties in the precise definitions of the terms in Eq. 2. For the RFA analysis, the points in

the vector \mathbf{y} come from voltage scan data. To determine the parameters independently, one should use several different voltage scans, which cover a wide range of beam conditions. Since a voltage scan is actually a measurement of the integrated energy spectrum, once should differentiate the signal to obtain a set of independent data points. These points may not individually have enough signal to be meaningful, so one can group them together (i.e. make energy “bins” of varying width) to get one element of the \mathbf{y} vector.

The choice of which simulation parameters to fit is also essential. There are many parameters that characterize the production of secondary electrons in POSINST [5], but a few stand out as being especially important. Among them are:

- **dtspk**, the peak true secondary electron yield
- **P1epk**, the low energy elastic yield
- **P1rinf**, the redifused yield at infinity
- **E0epk**, the energy at which peak secondary production occurs
- **powts**, the “shape parameter,” which determines the rise and fall of the SEY curve
- **pangsec**, the angular distribution of secondary electrons
- **enpar** and **pnpars**, which determine the energy distribution of secondary electrons

In general, primary photoelectrons are less well understood than secondary electrons. Some important primary emission parameters include:

- **queffp**, the quantum efficiency
- **ek0phel** and **eksigphel**, the peak energy and width of the photoelectron energy distribution
- **refleff**, the photon reflectivity

Generally speaking, **dtspk** and **queffp** need to be included in the fitting procedure to get good agreement with the RFA data. Other strong parameters include **P1epk**, **P1rinf**, and **powts**, but they are highly correlated with each other (i.e. have similar effects on the RFA simulation), so only one of the three is needed.

The starting points for several SEY parameters (**dtspk**, **E0epk**, **powts**), were chosen based on fits to the in-situ SEY measurements in CESR [7].

We have found that in order to have any RFA signal for a high current electron beam, one needs to produce some high energy photoelectrons. Currently this is accomplished by using a Lorentzian photoelectron energy distribution (rather than the default Gaussian distribution), with a low peak energy (**ek0phel** = 10eV), but a large width (**eksigphel** = 150 eV). However, the drift RFA data does not seem to constrain the exact shape of the distribution. Measurements with a shielded pickup detector [3] provide a method to probe these parameters in more detail.

The photon flux and reflectivity at the RFA are fixed, based on a 3 dimensional simulation of photon production and reflection in the CESRTA vacuum chamber [8], which includes diffuse scattering and a realistic model of the CESR vacuum chambers. Photoelectron parameters were allowed to be different for different beam energies and species, because the photon energy spectrum at any given location in CESR will be different for the two species.

In order to get a good fit to the data, one should choose parameters which have a strong effect on the simulations, and are relatively independent of each other. We have found that a reasonable fit can be obtained with as little as three parameters- typically the true secondary yield (**dtspk**), elastic yield (**P1epk**), and quantum efficiency (**queffp**). The true secondary yield has the strongest effect on data taken with short bunch spacings, high bunch currents, and positron beams. The elastic yield, meanwhile, is best determined by data with large bunch spacing, while the quantum efficiency prefers low beam current. Table IV gives a list of data sets used in one round of fitting, and indicates which parameter is most strongly associated with it.

Several sources of error must be taken into account when constructing the error matrix (**W** in Eq. 1). They include:

- Noise in the measurements (typically quite small)
- Statistical errors in simulations. This is a major source of error. It can be reduced by increasing the number of macroparticles used in the simulation, at the cost of increased the run time.
- A general error of 10% was added to account for systematic uncertainties in the data. One such uncertainty is unevenness in bunch currents along the train, which is not accounted for in the simulation.
- We have observed a slow drift of baseline (zero current value) in measurements, on the order of $\sim 2\%$ of full scale. This amounts to $\sim 20\text{nA}$ on the lowest gain setting, and $\sim .02\text{nA}$ on the highest one.
- An extra 20% error was added to signal in the simulation caused by beam pipe hole secondaries, to

account for uncertainty in the modeling of this phenomenon.

- Since the gradient for Jacobian matrix (**X**) is determined by simulation, it will also have an associated error. This cannot be included in the **W** matrix, because it will be different for each parameter. However, it can still be calculated, and its effect on the final parameter errors can be estimated.

We have found that, in general, one can obtain a reasonable fit to the data with only three (well chosen) parameters. As mentioned above, one good set consists of the true secondary yield, elastic yield, and quantum efficiency. Using more parameters does allow for a slightly better fit, at the cost of uniqueness and clarity.

Fig. 22 shows some of the results of the parameter finding method for an uncoated aluminum drift chamber. The plots compare the data and simulation for the signal across the 9 RFA collectors at three different retarding voltages. Overall there is good agreement between data and simulation for a wide variety of beam conditions.

In principle, errors on the final parameter values are readily obtainable during the course of the analysis. The covariance matrix for the parameters is $(\mathbf{X}^T \mathbf{W} \mathbf{X})^{-1}$. Standard errors on each parameter can be derived from the diagonal elements of the covariance matrix, and the correlations between each parameter from the off-diagonal elements. However, it should be noted that this analysis will only seek out the nearest local minimum in parameter space. It is always possible that a better fit can be achieved with a different set of values, especially if one uses many parameters in the fit. Therefore, these errors should be understood as the width of the local minimum, rather than an absolute determination of the uncertainty in the parameter. Nonetheless, the ability of this method to achieve a good fit for data taken under a wide variety of beam conditions strongly implies that the PEY and SEY models used are reproducing reality to a reasonable degree.

The best fit values and confidence intervals for an Aluminum chamber are shown in Table V. This chamber was installed in the 15W location (see Section IV), and the fit used the data taken during May 2010 (listed in Table IV). The values listed for the error bars also include an estimate of the uncertainty introduced by errors in the Jacobian matrix, which is added in quadrature to the standard error. Table VI lists the best fit values for the 15E amorphous Carbon coated chamber, using the same data sets. Finally, Table VII gives the values for a TiN coated chamber, installed at 15W during December 2010. As mentioned above, the starting point for all the listed SEY parameters were taken from fits to measured in-situ data. It is worth noting that this analysis indicates a very low secondary yield for both coated chambers.

One somewhat strange result of this analysis is that the quantum efficiency at 2.1GeV was found to be quite low for positron beams at 15E, and electron beams at 15W.

TABLE IV: List of beam conditions used for one round of fitting, and which parameter(s) they help determine

Bunches	Bunch current	Species	Bunch Spacing	Beam Energy	Parameter(s)
45	2.3	e+	14	2.1	dtspk
20	2.8	e+	4	4	dtspk
20	7.5	e+	14	2.1	dtspk
20	2.95	e+	14	4	dtspk
45	2.67	e+	14	5.3	dtspk
45	1.25	e+	4	5.3	dtspk
45	2.89	e-	4	5.3	dtspk, queffp
20	2.6	e-	14	2.1	queffp
45	0.8	e-	14	5.3	queffp
45	0.75	e+	14	5.3	queffp
45	0.75	e-	14	2.1	queffp, P1epk
9	3.78	e+	280	2.1	queffp, P1epk
45	0.75	e+	14	4	queffp, P1epk
9	3.78	e-	280	2.1	P1epk
9	3.78	e-	280	5.3	P1epk
9	3.78	e+	280	4	P1epk
9	4.11	e+	280	5.3	P1epk

TABLE V: Best fit parameters- 15W aluminum chamber

Parameter	Base Value	Final Value
dtspk	1.37	$1.74 \pm .02$
P1epk	.5	$.43 \pm .01$
P1rinf	.2	.2
E0epk	280eV	280eV
powts	1.54	1.54
queffp, 2.1GeV, e+	.1	$.034 \pm .004$
queffp, other	.1	$.111 \pm .006$

TABLE VI: Best fit parameters- 15E amorphous carbon coated chamber

Parameter	Base Value	Final Value
dtspk	.76	$.55 \pm .02$
P1epk	.5	$.29 \pm .02$
P1rinf	.2	.2
E0epk	300eV	300eV
powts	1.77	1.77
queffp, 2.1GeV, e+	.1	$.021 \pm .003$
queffp, other	.1	$.081 \pm .017$

The value for the other species, and for 4 and 5.3GeV, are all consistent with each other. The anomalous value is quoted separately from the other best fit values. This discrepancy appeared for both the 15W Al chamber and the 15E carbon coated chamber (it did not appear for the 15W TiN chamber, because no 2.1GeV electron beam data was used in the fit). It is most likely a reflection of the incompleteness of our photon and photoelectron modeling.

VII. CONCLUSIONS

Retarding field analyzers have been installed in drift regions around CESR, and a great deal of has been col-

TABLE VII: Best fit parameters- 15W TiN coated chamber

Parameter	Base Value	Final Value
dtspk	.73	$.54 \pm .01$
P1epk	.5	$.36 \pm .01$
P1rinf	.2	.2
E0epk	370eV	370eV
powts	1.32	1.32
queffp	.1	$.068 \pm .007$

lected with them. These data have been used to directly compare the efficacy of various electron cloud mitigating coatings. Detailed model of our RFAs have been developed, and integrated into the cloud simulation code POSINST, enabling analysis on a more quantitative level, and resulting in best fit simulation parameters, which describe the detailed performance of each material in situ.

Future work includes detailed analysis of RFA data taken in dipole, quadrupole, and wiggler field regions, as well as comparison with other cloud measurement techniques.

APPENDIX A: ADDITIONAL MITIGATION COMPARISONS

-
- [1] R. A. Rosenberg and K. C. Harkay, Nucl. Instrum. Methods Phys. Res. **A453**, 507 (2000).
- [2] M. A. Palmer, M. G. Billing, J. R. Calvey, G. W. Codner, S. Greenwald, Y. Li, X. Liu, J. A. Livezey, R. E. Meller,

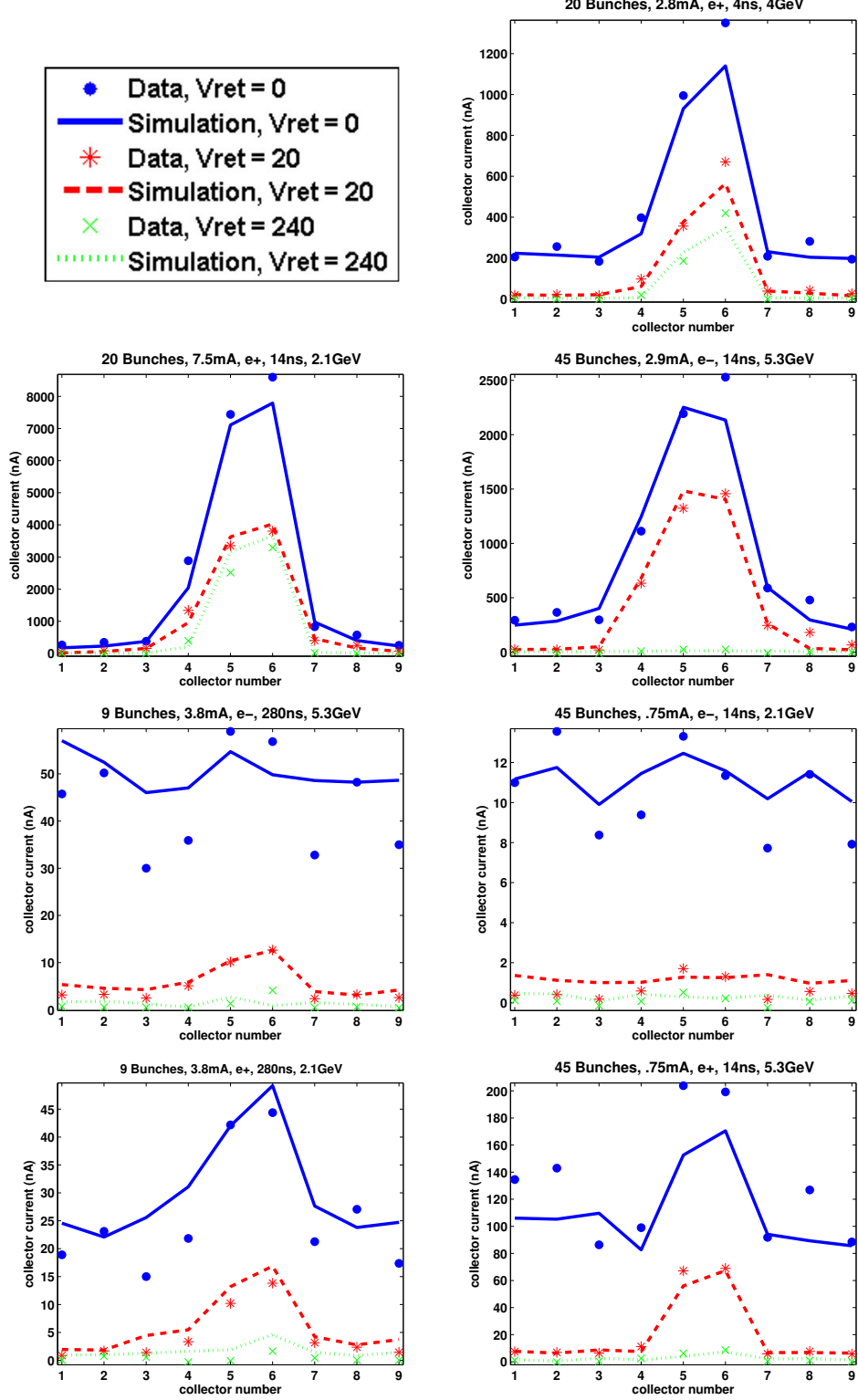


FIG. 22: Comparison of RFA data and simulation, using best fit parameters. The plots show the signal across the 9 RFA collectors at three different retarding voltages.

- R. M. Schwartz, et al., in *Proceedings of the 2009 Particle Accelerator Conference, Vancouver, BC* (2009), pp. 3510–3512, URL <http://accelconf.web.cern.ch/AccelConf/PAC2009/papers/th5rfp030.pdf>.
- [3] J. A. Crittenden, Y. Li, X. Liu, M. A. Palmer, J. P. Sikora, S. Calatroni, and G. Rumolo, in *Proceedings of the 2011 Particle Accelerator Conference, New York, NY* (2011), pp. 1752–1754, URL <http://accelconf.web.cern.ch/AccelConf/PAC2011/papers/wep142.pdf>.
- [4] Y. Suetsugu, K. Kanazawa, K. Shibata, H. Hisamatsu, K. Oide, F. Takasaki, R. V. Dostovalov, A. Krasnov, K. V. Zolotarev, E. S. Konstantinov, et al., *Nucl. Instrum. Methods Phys. Res. A* **554**, 92 (2005).
- [5] M. A. Furman and M. T. F. Pivi, *Phys. Rev. ST Accel. Beams* **5**, 124404 (2002).
- [6] J. R. Calvey, J. A. Crittenden, G. F. Dugan, M. A. Palmer, M. Furman, and K. Harkay, in *Proceedings of the 2011 Particle Accelerator Conference, New York, NY* (2011), pp. 501–503, URL <http://accelconf.web.cern.ch/AccelConf/PAC2011/papers/mop214.pdf>.
- [7] J. Kim, D. Asner, J. Conway, S. Greenwald, Y. Li, V. Medjizade, T. Moore, M. Palmer, and C. Strohman, in *Proceedings of ECLOUD 2010: 49th ICFA Advanced Beam Dynamics Workshop on Electron Cloud Physics, Ithaca, NY*, edited by K. Smolenski (in press).
- [8] G. Dugan and D. Sagan, in *Proceedings of ECLOUD 2010: 49th ICFA Advanced Beam Dynamics Workshop on Electron Cloud Physics, Ithaca, NY*, edited by K. Smolenski (in press).